Ultra-sensitive planoconcave optical microresonators for ultrasound sensing

James A. Guggenheim[1,], Jing Li[1], Thomas J. Allen[1], Richard J. Colchester[1], Sacha Noimark[2], Olumide Ogunlade[1], Ivan P. Parkin[2], Ioannis Papakonstantinou[3], Adrien Desjardins[1], Edward Z. Zhang[1], and Paul C. Beard[1]

[1]Department of Medical Physics and Biomedical Engineering, University College London, Gower Street, London, WC1E 6BT, UK

[2]Department of Chemistry, University College London, Gower Street, London, WC1E 6BT, UK

[3]Department of Electronic and Electrical Engineering, University College London, Gower Street, London, WC1E 6BT, UK

Exquisitely sensitive broadband detectors are needed to expand the capabilities of biomedical ultrasound, photoacoustic imaging and industrial ultrasonic non-destructive testing techniques. Piezoelectric transducers are near ubiquitous but achieving high sensitivity requires large element size and resonant material compositions leading to narrow directivity, poor frequency response characteristics and ultimately compromised image signal-to-noise-ratio and quality. Here, a generic new optical ultrasound sensing concept based on a novel planoconcave polymer microresonator is described. This achieves strong optical confinement (Q-factors>10^5) resulting in very high sensitivity with excellent broadband acoustic frequency response and wide directivity. The concept is highly scalable in terms of bandwidth and sensitivity. To illustrate this, a family of microresonator sensors with broadband acoustic responses up to 40MHz and noise-equivalent-pressures as low as 1.6mPa/√Hz have been fabricated and comprehensively characterized in terms of their acoustic performance. In addition, their practical application to high resolution photoacoustic and ultrasound imaging is demonstrated. The highly favorable acoustic performance and design flexibility of the technology offers new opportunities to advance biomedical and industrial ultrasound based techniques.

The sensitive detection of broadband ultrasound waves in the hundreds of kHz to tens of MHz range underpins techniques such as biomedical photoacoustic tomography and microscopy[1,2], clinical ultrasound imaging[3] and industrial non-destructive evaluation and monitoring[4–6]. Piezoelectric ultrasound receivers represent the current state of the art but present two key acoustic performance limitations. Firstly, achieving the high acoustic sensitivities required for large imaging depths necessitates piezoelectric element sizes on a millimetre-centimetre scale which result in a highly directional response at MHz frequencies due to spatial averaging. This can have the counter-productive effect of degrading image SNR and fidelity in paradigms such as photoacoustic tomography or synthetic aperture pulse-echo ultrasound which require sub-wavelength detectors with a near omnidirectional response. Secondly, achieving the very highest sensitivities typically requires detectors that are fabricated from acoustically resonant piezoceramic materials. This can result in a sharply peaked frequency response thereby precluding a faithful representation of the incident acoustic wave and ultimately compromising image fidelity.

Optical ultrasound sensors offer an alternative that is beginning to challenge the current piezoelectric dominated landscape[5,7–17]. This applies particularly to devices based on highly sensitive optically resonant structures such as micro-rings[9,10], Fabry-Pérot etalons[5,7,12,14,17] and in-fibre Bragg gratings[13]. In terms of acoustic performance alone, their attraction is twofold. Firstly, extremely high sensitivity is theoretically possible due to the interaction length scaling provided by optically resonant structures. Secondly, they offer the prospect of low directional sensitivity at MHz frequencies since the acoustic element size is optically defined and can approach the micron-scale optical diffraction limit. However, it has proved challenging to realise both high sensitivity and wide directivity along with a uniform broadband frequency response, particularly with devices that can be scaled to achieve the high channel counts required for imaging applications. In this study, a new

generation of optical ultrasound sensors based on a high Q plano-concave microresonator that has the potential to meet these requirements is described. As well as excellent acoustic characteristics, a key distinguishing feature of this approach over existing methods is the design flexibility it offers allowing the acoustic performance to be finely tuned to match a wide range of applications. This enables realisation of a broadly applicable family of highly sensitive, micron scale broadband ultrasound sensors with unprecedented acoustic performance and versatility for biomedical and industrial ultrasound.

The sensors are based upon a solid planoconcave polymer microcavity formed between two highly reflective mirrors (R>98%) which is embedded in a layer of matching polymer so as to create an acoustically homogeneous planar structure as illustrated in figures 1a-b. The cavity is constructed by depositing a droplet of optically clear UV-curable liquid polymer onto a dielectric mirror coated polymer substrate (see methods). The droplet stabilises to form a smooth spherical cap under surface tension and is subsequently cured under UV-light. The second dielectric mirror coating is then applied, followed by the addition and curing of further polymer to create the encapsulating layer.

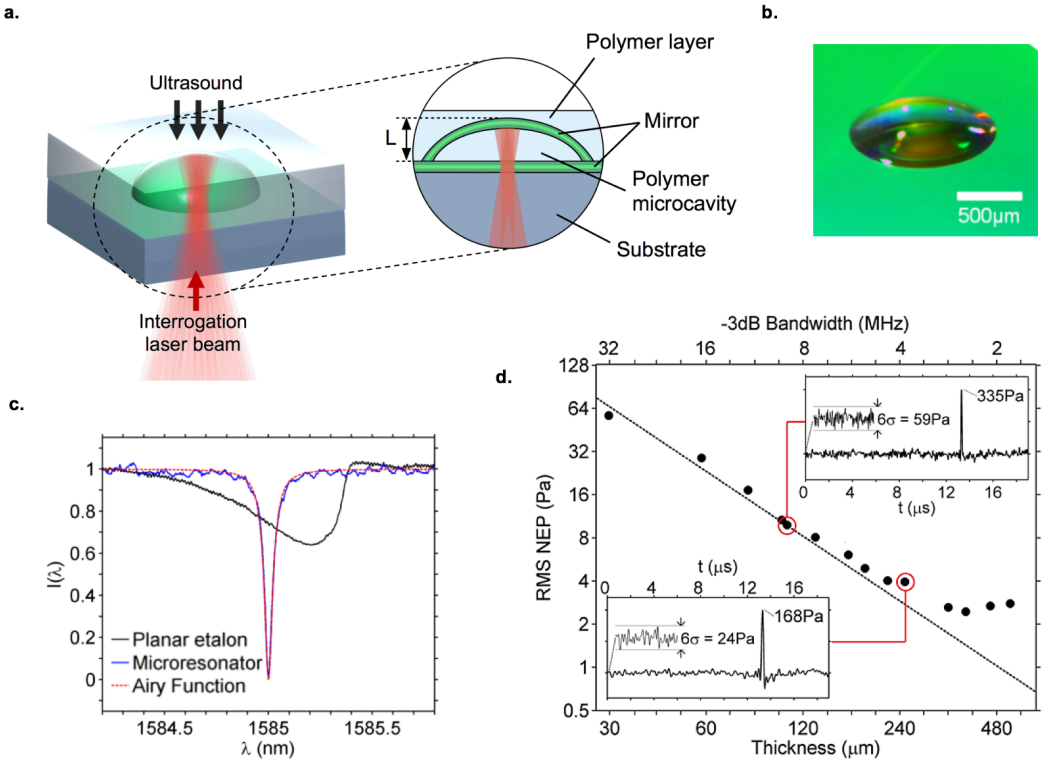

Figure 1 | Planoconcave optical microresonator ultrasound sensor. a, Sensor schematic (L = cavity thickness). The sensor comprises a planoconcave polymer microcavity encapsulated in a planar polymer layer. **b,** Photograph of polymer microcavity prior to application of the encapsulating polymer layer. **c,** Measured cavity transfer function of a planoconcave microresonator sensor (Q=30,000, finesse=148, visibility=0.96) and a planar fused silica etalon (Q=3,300, finesse=17, visibility=0.22) of equal thickness (100µm) and reflectivity (98%), measured with the same interrogation laser beam waist ($\omega_0 = 12.5$µm, where w_0 is the $1/e^2$ beam radius). **d,** RMS noise-equivalent pressure (NEP) over a measurement bandwidth equal to the -3dB bandwidth of each sensor, except for the 30µm sensor for which the measurement bandwidth was 20MHz (see methods). The dotted line shows the expected trend with sensitivity increasing with thickness. Inset figures show extracts from the acoustic waveforms (original length 200µs) measured by 100µm (Q=64,000) and 250µm (Q=108,000) thick sensors in response to a plane wave monopolar acoustic pulse produced by a laser ultrasound source (see methods). The temporal pulse widths of the measured waveforms are 81ns for the 100µm sensor and 165ns for the 250µm sensor (the values quoted are the full width half maxima of the pulses). The zoomed in sections of the noise show 6 times the root-mean-squared value (RMS).

The sensor is operated by illuminating it with a focussed continuous-wave laser beam at a wavelength λ_b tuned to the edge of the cavity resonance. Under these conditions, the stress due to an incident acoustic wave modulates the cavity optical thickness producing a corresponding modulation in the reflected optical power which is detected by a photodiode. The magnitude of the reflected power modulation, and thus the sensitivity of the sensor, is dependent upon the sharpness of the resonance. In order to optimise this, the cavity geometry is carefully designed such that when illuminated by a tightly focussed interrogation laser beam, the top mirror curvature is perfectly matched to that of the diverging beam. This precisely corrects for the divergence by refocussing the light upon each round trip and preventing the beam from walking off laterally as it would in a planar etalon. As a consequence, it is possible to achieve a very high degree of optical confinement as demonstrated in figure 1c, which shows the cavity transfer function (CTF) of a 100µm thick planoconcave microresonator sensor of 98% mirror reflectivity interrogated with a 12.5µm beam waist. The CTF is extremely sharp with a very high Q-factor of 30,000, moreover it is near-indistinguishable from the Airy function; the theoretical CTF for a perfectly confined optical field. For comparison, also plotted in figure 1c is the CTF of a planar etalon of the same thickness and mirror reflectance interrogated with an identical beam waist. The planar etalon CTF bears little resemblance to the Airy function, with a distorted asymmetric shape[18], an order-of-magnitude lower Q-factor and poor visibility due to the beam walk-off arising from the limited optical confinement in the planar cavity. This illustrates the key advantage of the planoconcave cavity over the well-established polymer planar Fabry-Pérot etalon ultrasound sensor[7]. The latter has been shown capable of providing excellent photoacoustic image quality[19]. However its sensitivity and thus imaging depth is limited by its relatively modest Q-factor due to the beam walk-off that arises when illuminated by a tightly focused laser beam as required to achieve small element size for low directional sensitivity.

The strong optical confinement afforded by the planoconcave microresonator design creates the opportunity to maximise sensitivity in two ways. The first is by increasing the mirror reflectivity, trapping light for longer and increasing the number of significant round trips in the cavity, leading to a higher Q-factor and thus a higher CTF gradient at λ_b. The second is by increasing the cavity thickness L. This results in a greater change in optical thickness for a given acoustic pressure since the sensor responds to the spatial average of the acoustic field. The latter results in a reduction in acoustic bandwidth with increasing L and the ensuing trade-off between sensitivity and bandwidth presents the opportunity to create a family of sensors optimised for different applications. By contrast, increasing either the reflectivity or the thickness of a planar etalon exacerbates beam walk-off thereby reducing the Q-factor and thus sensitivity. To illustrate the sensitivity-bandwidth scaling of the concept, a family of 14 sensors were designed and fabricated with different thicknesses ranging from 30µm to 530µm and a maximum mirror reflectivity of 99.3%. The sensors were characterised in terms of their sensitivity, frequency response, and directivity.

Sensitivity was assessed by measuring the noise equivalent pressure (NEP), which was estimated for each sensor based on its response to a broadband (1-70MHz) monopolar acoustic pulse produced by a plane wave laser ultrasound source (see methods). The pressure output of the source was calibrated with reference to a primary standard, certified by the UK National Physics Laboratory. NEP values are quoted without signal averaging and for a measurement bandwidth equal to the -3dB bandwidth of the sensor under test. To illustrate the scaling of NEP with sensor thickness, figure 1d shows the NEP of all 14 sensors, also indicating the reducing bandwidth as well as example acoustic waveforms obtained using the 100µm and 250µm thick sensors (inset figures). As expected, figure 1d shows that the NEP improves with increased thickness (and decreased bandwidth) for L<250µm. For example, the NEP of the 100µm sensor is 9.8Pa (over an 8.9MHz measurement bandwidth, 3.3mPa/√Hz) and that of the 250µm sensor is lower at 4Pa (over a 3.8MHz measurement bandwidth, 2mPa/√Hz). For L>250µm the improvement in NEP declines and reaches a plateau. This is due to a combination of several factors including optical absorption in the cavity, laser phase noise, and mismatches between the curvature of the concave surface of the cavity and that of the beam. The minimum NEP obtained is that of the 340µm thick sensor at 2.6Pa (over a 2.8MHz measurement bandwidth, 1.6mPa/√Hz). This very low NEP is approximately an order-of-magnitude better than that of the planar Fabry-Pérot sensor[7]. Moreover, it is comparable to that reported for high sensitivity piezoelectric transducers used for deep tissue photoacoustic breast imaging that are four or five orders-of-magnitude greater in acoustic element size[20] and exhibit significantly poorer acoustic frequency response and directivity as discussed below.

As well as high sensitivity, a smooth well behaved frequency response that is sufficiently broadband to capture all relevant frequencies in an acoustic pulse is important. If this criterion is not met, as in the case of most piezoceramic transducers, waveforms and reconstructed images can be distorted. The planoconcave microresonator sensor is specifically designed such that it forms an acoustically homogeneous, semi-infinite polymer structure as shown in figure 1a. In conjunction with the good acoustic impedance matching to both the polymer backing substrate and the surrounding coupling medium, this design minimises internal acoustic reflections. A uniform, smooth frequency response characteristic of an acoustically non resonant broadband detector can therefore be expected. Figure 2a shows the measured responses of a representative subset of four sensors, measured using the same broadband laser ultrasound source described above (see methods). The response is indeed smooth in all cases, with a gradual roll-off to the first zero which occurs at the frequency at which the acoustic wavelength is exactly equal to the cavity thickness and in excellent agreement with theory [21]. The broadband nature of the frequency response is further illustrated by the waveforms in figure 1d. These show clean monopolar signals, free from artefacts or ringing, with the shorter pulse duration of the 100µm sensor signal (81ns) relative to that of the 250µm sensor signal (165ns) consistent with the broader bandwidth of the former.

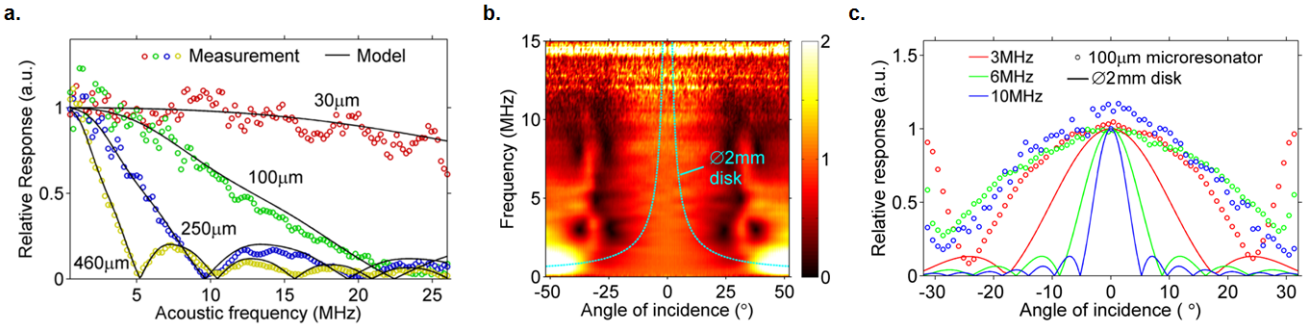

Figure 2 | Acoustic frequency response and directivity a, Measured frequency response for a range of sensors of different thickness compared with model data[21]. **b,** 100µm sensor directional response map (normalised to θ=0°) with contour line showing the 50% cut-off for the modelled response of a disk-shaped purely spatially averaging sensor of diameter 2mm. **c,** Directional response of 100µm sensor at selected frequencies as compared to the modelled response of a disk-shaped spatially averaging receiver of diameter 2mm. For all data: $\omega_0 = 12.5$µm.

Along with the NEP measurements in figure 1, the frequency response data in figure 2 illustrates the design flexibility of the concept. The frequency response of the 30µm sensor demonstrates that it is possible to obtain very broad bandwidths, on the order of tens of MHz, as required for high-resolution imaging applications such as photoacoustic microscopy and endoscopic ultrasound. At the other end of the scale, the most sensitive sensors (NEP <5Pa) with cut-off (first null) frequencies up to 10MHz or less lend themselves to cm scale deep tissue photoacoustic and ultrasound imaging; for example, broadband ultrasound signals traversing 3cm or more of breast tissue are bandlimited by frequency dependent acoustic attenuation to the extent that their frequency content beyond 5MHz is negligible[22]. At this length scale, the signals are also very weak (a few Pascals or less) so this case is very well-matched to the thick, low-frequency microresonator sensors that offer the highest sensitivity.

The complete characterisation of an ultrasound receiver requires measuring its directional response which to a first approximation is defined by its element size. The directivity is of critical importance for imaging techniques such as photoacoustic tomography and diagnostic ultrasound imaging which employ back projection, phased array or other synthetic aperture methods that require point-like omnidirectional receivers. Poor directivity (non-smooth or with a narrow angular range) not only introduces image artefacts but can seriously compromise image SNR[22]. Figure 2b shows the directivity of the 100µm planoconcave microresonator sensor measured using the laser ultrasound source (see methods). This example is chosen as representative since all of the sensors were interrogated with the same laser beam waist which (to a first approximation) defines the acoustic element size. The response exhibits a well behaved smooth roll-off from normal incidence to minima between 25 and 30°. Beyond these minima the response is more variable though there is strong sensitivity at

most angles and frequencies up to the extent of the measurement at ±52° and 15MHz. To put this into perspective, in order to achieve a sensitivity comparable to that of the 100µm microresonator sensor, it is estimated that a circular piezoelectric PVDF receiver (which, being fabricated from a polymer has comparable broadband frequency response characteristics to the microresonator sensor and thus provides a fair comparison) would require an element diameter of 2mm (see methods). For a receiver of this size, a highly frequency-dependent and relatively narrow directional response can be expected. This is shown in figure 2b and 2c which compare the modelled directional response of a 2mm diameter circular ultrasound receiver with the measured directivity of the 100µm microresonator (see methods). The microresonator provides a superior directivity in that its response is significantly less directional. This is particularly evident at higher frequencies; for example, at 10MHz, the angle of the first minimum of the 100µm thick microresonator sensor is 30° compared to 5° for the 2mm circular receiver. Note that the modelled response of the 2mm receiver is a best case scenario since it is based on the assumption that its directivity is defined by spatial averaging alone. In practice, additional acoustic interactions influence the directivity of real PDVF receivers resulting in an even more directional response than indicated in figure 2b[16].

The concept offers not only excellent broadband acoustic performance but flexibility of implementation. In addition to the above free-space sensors which can in principle be replicated to form 2D imaging arrays, the microresonator can also be formed on the tip of a single mode optical fibre to realise a highly miniaturised flexible probe-type ultrasound receiver. This is illustrated in figure 3 (a-b). In this example, we sought to further illustrate the high frequency scaling capability of the concept by forming a reduced cavity thickness (L=16um) compared to those described above. The NEP at 3.5MHz is 9.3Pa over a 20MHz measurement bandwidth (2.1mPa/√Hz) and, as shown in figure 3c, the response is broadband extending to approximately 40MHz. The response is less uniform than those of the free space devices in figure 2a owing to acoustic diffraction around the fibre tip, a common feature of probe-type ultrasound receivers[16]. The measured directivity (fig3d-e) shows that the sensor is effectively omnidirectional, with high sensitivity up to ±90°, for most frequencies up to 40MHz. It is assumed that this is due in part to the small illuminating beam radius (ω_o=5.2µm), however a detailed theoretical understanding and modelling of the directivity is required to fully interpret these results and will form the basis of future work.

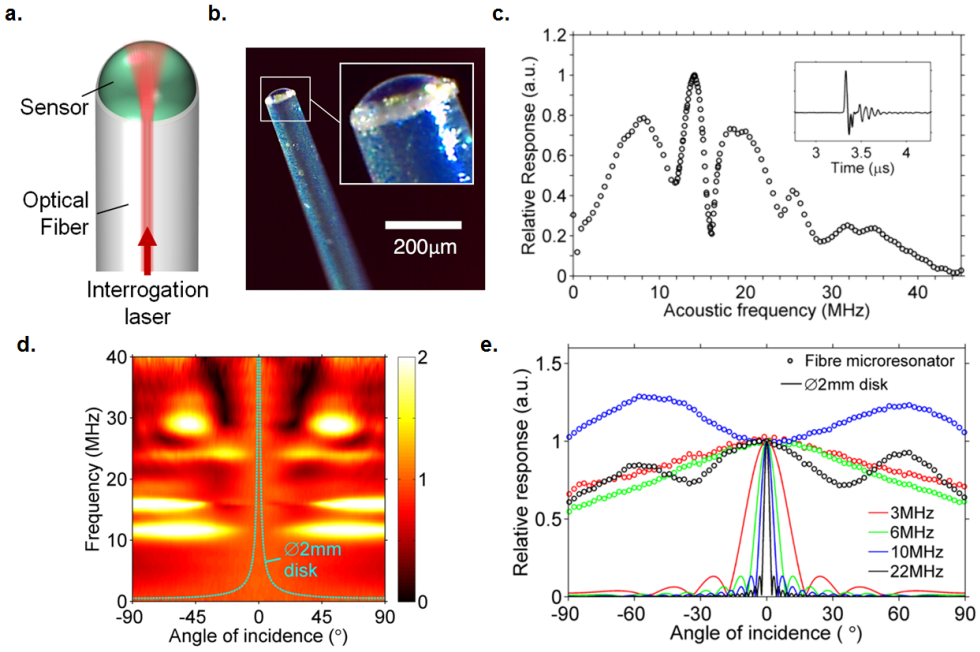

Figure 3 | Optical fibre microresonator sensor. a, schematic. **b,** photograph. **c,** frequency response. Inset shows time domain waveform in response to the laser ultrasound source (see methods). **d,** directional response map (normalised to θ=0°) with contour line showing the 50% cut-off for the modelled response of a disk-shaped purely spatially averaging sensor of diameter 2mm. **e,** directional response at selected frequencies as compared to the modelled response of a disk-

shaped spatially averaging sensor of diameter 2mm. Data is shown for a 16µm thick planoconcave optical microresonator fibre sensor.

To demonstrate practical applicability to photoacoustic and ultrasound imaging, two exemplars chosen to illustrate the benefits of the high broadband sensitivity and wide directivity provided by the technology are shown in figure 4. For ease of implementation, fibre microresonator type sensors were used in these demonstration examples.

Figure 4a.b shows an optical-resolution photoacoustic microscopy (OR-PAM) image[23] of the mouse ear acquired *in vivo* showing the microvasculature at the level of individual capillaries. This image was obtained by scanning a pulsed focussed photoacoustic excitation laser beam of 7 µm full-width-half-maximum over an 8mm x 8mm area and recording the photoacoustic signals at each scan point with the sensor in a fixed position at the centre of the scan area[24]. The fibre sensor was located at a distance of 1.2mm from the skin surface and ultrasound gel was used as the acoustic coupling medium. The high-contrast and large field-of-view demonstrate the high sensitivity and near omnidirectional response of the sensor. The latter is most apparent in the observation that at the lateral extremities of the scan area the sensor is recording photoacoustic waves with a frequency content up to 40 MHz over an angular aperture of 75 degrees. The implementation in figure 4 not only illustrates the favorable acoustic performance of the sensor. It also illustrates a potential route to achieving fast OR-PAM image acquisition over large areas since the near omnidirectional response of the sensor allows it to remain stationary, thereby obviating the need for time consuming mechanical scanning often used in conventional OR-PAM[25].

Figure 4c.d shows the second application example, a 3D high resolution pulse-echo ultrasound image of an *ex vivo* porcine aorta sample. The image was obtained by raster scanning a fibre microresonator sensor and a fibre-based laser ultrasound source (see methods) emitting broadband ultrasound pulses with a frequency content extending to 30MHz. The returning echoes from subsurface tissue structures are recorded by the fibre sensor and the 3D image was reconstructed using the k-wave toolbox[26]. The image shows the inner layered structure of the aorta wall and an ancillary branch departing the main vessel wall. The high resolution and spatial fidelity of this image further illustrate the benefits of the sensitive omnidirectional characteristics of the sensor since this imaging approach falls in the category of synthetic aperture techniques that require detection over a large angular aperture.

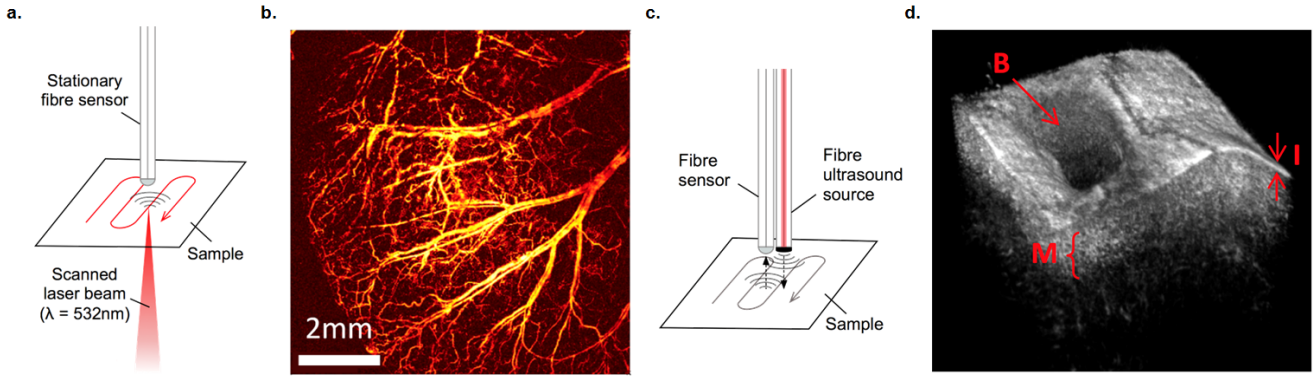

Figure 4 | Imaging demonstrations. a, schematic of fibre-microresonator sensor based optical resolution photoacoustic microscopy (OR-PAM) experiment. **b,** OR-PAM image of mouse ear vasculature *in vivo*. The scan area was 8mm x 8mm with a 20µm step-size which defines the lateral resolution. The excitation laser beam diameter (FWHM) was 7µm, λ = 578nm, with a 1.2ns pulse-duration, pulse repetition frequency (PRF) of 5 kHz and 800 nJ pulse energy. The objective lens focal length was 50 mm. Image acquisition time was ≈5 mins. Sensor bandwidth: 40MHz (L=16µm). Vertical resolution is defined by the FWHM of the impulse response function (inset figure 3(c)) and was 36µm. Typical image SNR values near to the centre and near to the edge are 141:1 (43.0 dB) and 28:1 (28.9 dB). **c,** schematic of all-fiber pulse-echo ultrasound experiment (performed in water). The fiber ultrasound source comprised an optical fiber (200µm core diameter) with a highly optically absorbing coating at its distal end irradiated with 1.2 ns laser pulses; the -6dB acoustic bandwidth of the

source was 29.2MHz. **d,** 3D pulse-echo ultrasound image of *ex vivo* porcine aorta, B = branching vessel, I = intima, M = media. The scan area was 1cm x 1cm with a 50µm step-size. Sensor bandwidth: 55 MHz (L=12µm). The lateral and axial resolutions were 94.2µm and 65.9µm respectively obtained by imaging a 7µm diameter carbon fibre.

In summary, a family of planoconcave optical microresonator ultrasound sensors have been developed that exploit strong optical confinement in order to deliver exquisite sensitivity. The concept offers several important advantages over the current state of the art. In terms of acoustic performance alone, it is the unparalleled combination of both high broadband sensitivity and wide angular detection aperture that most obviously distinguishes it. This is most compellingly illustrated by the remarkable result in figure 4 in which the fibre optic microresonator sensor exhibits a near omnidirectional response at frequencies up to at least 40MHz with an NEP of just 10Pa; a level of acoustic performance that significantly outperforms current piezoelectric or optical ultrasound detection technology. Achieving comparable directivity using a piezoelectric receiver for example would require an element size on the order of 10µm which would be several orders of magnitude less sensitive. As mentioned previously, isotropic detection is of crucial importance for achieving high SNR with imaging techniques such as photoacoustic tomography or 3D pulse-echo synthetic aperture ultrasound. The favourable combination of high sensitivity and directivity of the microresonator sensors could therefore pave the way to extending the penetration depth of these imaging modalities. Moreover, the combination of wide directivity and uniform broadband frequency response offers the prospect of better image quality than achievable with current optical and piezoelectric based ultrasound detection methods.

The technology offers significant design flexibility and scalability. Increasing the mirror reflectivities to increase Q-factor along with the use of lower phase noise lasers or phase compensation techniques may provide opportunities to further increase sensitivity potentially to the sub-Pa regime. Bandwidth can be adjusted by appropriate selection of the cavity thickness. In this study sensors with bandwidths in the 1-40MHz range were demonstrated since this frequency range encompasses most biological and industrial applications. However, higher frequency devices extending beyond 100MHz for ultra-high resolution applications can in principle be fabricated by forming a thinner cavity. The sensitivity-bandwidth scaling offered by the concept lends itself to a wide range of applications from high resolution endoscopic clinical photoacoustic and ultrasound imaging enabled by microresonator sensors operating at tens of MHz frequencies to sensors designed to operate in the low MHz range with extremely high sensitivity for deep tissue photoacoustic imaging. Although this study has focussed on detection at MHz frequencies, the sensors are responsive to lower frequencies, in principle down to dc. This offers additional opportunities for passive acoustic emission sensing in industrial testing, machining and process monitoring applications[6] which typically require detection at sub-MHz frequencies. The technology also offers versatility and flexibility of implementation. Feasibility has been demonstrated using individual free-space devices with relatively large footprints but it is anticipated that these can be truncated to the width of the interrogation laser beam (the active part of the sensor; ≈30 µm) and replicated at low cost to create high density 2D imaging detector arrays using polymer fabrication methods such as inkjet printing, nanoimprinting and UV embossing previously developed for microlens array fabrication[27]. Such arrays could then be optically addressed by single or multi-beam optical scanning or using structured full field illumination. Moreover, as demonstrated, the microresonators can be formed at the tip of an optical fibre in order to realise an inexpensive, flexible, highly miniaturised probe type receiver for endoscopic medical applications or limited access industrial ultrasonic NDE and acoustic emission sensing. Low cost for disposable use, electrical passivity and immunity to EMI permitting operation in electromagnetically noisy environments such as MRI scanners or hostile industrial process facilities provide further advantages. Finally, all of the sensors described were fabricated using dichroic dielectric coatings that are transparent in the 600-1200nm wavelength range allowing the convenient backward-mode[7] of photoacoustic imaging and sensing to be realised.

In conclusion, this concept offers a new and versatile generic approach to high performance ultrasound detection with the potential to extend the capabilities of a wide range of biomedical and industrial photoacoustic and ultrasound imaging and sensing techniques.

Acknowledgements

This work was supported by the Engineering and Physical Sciences Research Council (EPSRC), the European Union project FAMOS (FP7 ICT, Contract 317744), the European Research Council through European Starting Grant 310970 MOPHIM, an Innovative Engineering for Health award by the Wellcome Trust (WT101957) and King's College London and University College London Comprehensive Cancer Imaging Centre, Cancer Research UK & Engineering and Physical Sciences Research Council, in association with the Medical Research Council and Department of Health, UK.

References

1. Beard, P. Biomedical Photoacoustic Imaging. *Interface Focus* **1,** 602–631 (2011).
2. Wang, L. V & Gao, L. Photoacoustic Microscopy and Computed Tomography: From Bench to Bedside. *Annu. Rev. Biomed. Eng.* **16,** 155–185 (2014).
3. Powers, J. & Kremkau, F. Medical ultrasound systems. *Interface Focus* **1,** 477–489 (2011).
4. Drinkwater, B. W. & Wilcox, P. D. Ultrasonic arrays for non-destructive evaluation: A review. *NDT E Int.* **39,** 525–541 (2006).
5. Fischer, B. Optical microphone hears ultrasound (Commentary). *Nat. Photonics* **10,** 356–358 (2016).
6. Grosse, Christian U., Ohtsu, M. (Eds). *Acoustic Emission Testing*. (Springer Science & Business Media, 2008).
7. Zhang, E., Laufer, J. & Beard, P. Backward-mode multiwavelength photoacoustic scanner using a planar Fabry-Perot polymer film ultrasound sensor for high-resolution three-dimensional imaging of biological tissues. *Appl. Opt.* **47,** 561–577 (2008).
8. Nuster, R., Slezak, P. & Paltauf, G. High resolution three-dimensional photoacoutic tomography with CCD-camera based ultrasound detection. *Biomed. Opt. Express* **5,** 2635 (2014).
9. Ling, T., Chen, S.-L. & Guo, L. J. High-sensitivity and wide-directivity ultrasound detection using high Q polymer microring resonators. *Appl. Phys. Lett.* **98,** 204103 (2011).
10. Li, H., Dong, B., Zhang, Z., Zhang, H. F. & Sun, C. A transparent broadband ultrasonic detector based on an optical micro-ring resonator for photoacoustic microscopy. *Sci. Rep.* **4,** 4496 (2014).
11. Paltauf, G., Nuster, R., Haltmeier, M. & Burgholzer, P. Photoacoustic tomography using a Mach-Zehnder interferometer as an acoustic line detector. *Appl. Opt.* **46,** 3352–3358 (2007).
12. Tadayon, M. A., Baylor, M. & Ashkenazi, S. Polymer waveguide Fabry-Perot resonator for high-frequency ultrasound detection. *IEEE Trans. Ultrason. Ferroelectr. Freq. Control* **61,** 2132–2138 (2014).
13. Rosenthal, A., Razansky, D. & Ntziachristos, V. High-sensitivity compact ultrasonic detector based on a pi-phase-shifted fiber Bragg grating. *Opt. Lett.* **36,** 1833–5 (2011).
14. Hajireza, P., Krause, K., Brett, M. & Zemp, R. Glancing angle deposited nanostructured film Fabry-Perot etalons for optical detection of ultrasound. *Opt. Express* **21,** 6391–400 (2013).
15. Yakovlev, V. V *et al.* Ultrasensitive Non-Resonant Detection of Ultrasound with Plasmonic Metamaterials. *Adv. Mater.* 1–6 (2013). doi:10.1002/adma.201300314
16. Hurrell, A. & Beard, P. C. in *Ultrasonic Transducers: Materials and Design for Sensors, Actuators and Medical Applications* (ed. Nakamura, K.) **94,** Chapter 9, pp619-676 (2012).
17. Preisser, S. *et al.* All-optical highly sensitive akinetic sensor for ultrasound detection and photoacoustic imaging. *Biomed. Opt. Express* **7,** 4171 (2016).
18. Varu, H. The optical modelling and design of Fabry Perot Interferometer sensors for ultrasound detection. *PhD Thesis, University College London* (University College London, 2014).
19. Jathoul, A. P. *et al.* Deep in vivo photoacoustic imaging of mammalian tissues using a tyrosinase-based genetic reporter. *Nat. Photonics* **9,** 239–246 (2015).
20. Xia, W. *et al.* An optimized ultrasound detector for photoacoustic breast tomography. *Med. Phys.* **40,** 32901 (2013).
21. Beard, P. C., Perennes, F. & Mills, T. N. Transduction mechanisms of the Fabry-Perot polymer film sensing concept for wideband ultrasound detection. *IEEE Trans. Ultrason. Ferroelectr. Freq. Control* **46,** 1575–1582 (1999).
22. Allen, T. J. & Beard, P. C. Optimising the detection parameters for deep-tissue photoacoustic imaging. in *Proc SPIE 8223* (eds. Oraevsky, A. A. & Wang, L. V.) **8223,** 82230P (2012).
23. Hu, S., Maslov, K. & Wang, L. V. Second-generation optical-resolution photoacoustic microscopy with improved sensitivity and speed. *Opt. Lett.* **36,** 1134–1136 (2011).
24. Xie, Z., Jiao, S., Zhang, H. F. & Puliafito, C. A. Laser-scanning optical-resolution photoacoustic microscopy. *Opt. Lett.* **34,** 1771–1773 (2009).
25. Yao, J. & Wang, L. V. Photoacoustic microscopy. *Laser Photon. Rev.* **7,** 758–778 (2013).
26. Treeby, B. E. & Cox, B. T. k-Wave: MATLAB toolbox for the simulation and reconstruction of photoacoustic wave fields. *J. Biomed. Opt.* **15,** 21314 (2010).
27. Ottevaere, H. & Cox, R. Comparing glass and plastic refractive microlenses fabricated with different technologies.

J. Opt. A … **407,** (2006).
28. Yuan, Y. & Lee, T. R. in *Surface Science Techniques* (eds. Bracco, G. & Holst, B.) **51,** 3–34 (Springer-Verlag, 2013).
29. Colchester, R. J. *et al.* Broadband miniature optical ultrasound probe for high resolution vascular tissue imaging. *Biomed. Opt. Express* **6,** 1502–1511 (2015).
30. Noimark, S. et al. Carbon-nanotube-PDMS composite coatings on optical fibres for all-optical ultrasound imaging. *Adv. Funct. Mater.* **In press,** (2016).
31. Bacon, D. Characteristics of a PVDF membrane hydrophone for use in the range 1-100 MHz. *IEEE Trans. sonics Ultrason.* **SU-29,** 18–25 (1982).
32. Yao, J. *et al.* Wide-field fast-scanning photoacoustic microscopy based on a water-immersible MEMS scanning mirror. *J. Biomed. Opt.* **17,** 80505 (2012).

Methods

Microresonator design and fabrication

To fabricate the free-space sensors, small volumes (nL - µL) of UV-curable adhesive or epoxy were deposited on to mirror-coated substrates yielding free-standing liquid spherical caps. Under these conditions, the contact angle is a constant based on the energetic properties of the specific surface and fluid within some range due to hysteresis[28]. Thus, varying the volume of fluid deposited allows the thickness to be adjusted. For invariant contact angle, this also changes the base radius which scales with thickness as illustrated in the table below which provides the dimensions of each fabricated free-space sensor. Deposition was performed using a robotic plotting machine (GIX Microplotter II, Sonoplot, Middleton, WI, U.S.A.), by hand using a simple stamp, or by dip-coating in the case of the fibre sensor, prior to curing. Dichroic mirror coatings were applied as described in reference [7].

L (µm)	Ø (mm)	ROC (mm)
30	0.39	0.63
58	0.66	0.96
81	0.66	0.71
103	1.36	2.29
107	1.35	2.17
131	2.28	5.03
166	1.34	1.43
187	1.73	2.10
220	1.62	1.60
249	2.28	2.74
340	2.47	2.41
385	3.60	4.40
459	4.55	5.88
529	5.35	7.02

Table 1 | Dimensions of free-space planoconcave microresonator sensors; *L* = thickness, *Ø* = base diameter (footprint), *ROC* = radius of curvature.

To establish the dimensions in Table 1, the sensor thickness was calculated from the (wavelength) free spectral range FSR_λ (extracted from the cavity transfer function; CTF) using the relationship:

$$\mathrm{FSR}_\lambda = \frac{\lambda_0^2}{2Ln} \qquad \text{Equation 1}$$

where λ_0 is the vacuum wavelength, L is the thickness and n is the refractive index. The in-plane diameter *Ø* was measured from (reflection) images obtained by the optical scanner. The sensor ROC was calculated based on the assumption that the sensor geometry was a perfect spherical cap using:

$$ROC = \frac{L^2+a^2}{2L} \qquad \text{Equation 2}$$

where a is the base radius (Ø/2).

Sensor interrogation

The free space sensors were interrogated by illuminating them with a focused laser beam (ω_o=12.5µm) provided by a tuneable continuous-wave laser source (Tunics T100S-HP/SCL, Yenista Optics). The interrogation beam was positioned using a two axis galvanometer-based scanner[7] and the reflected beam from the sensor detected using a custom-designed AC and DC-coupled[7] InGaAs photodiode (G9801-22, Hamamatsu). The fibre

sensors were directly coupled to the interrogation laser and photodiode via an optical circulator (6015-3-APC, Thorlabs).

Noise equivalent pressure measurements

The noise-equivalent pressure (NEP) is the pressure that provides a signal-to-noise ratio (SNR) of unity in the low frequency limit where the acoustic wavelength is much larger than the cavity thickness and the frequency response is flat[2,7,21]. The NEP therefore represents the minimum detectable pressure and is given by

$$NEP = N/\psi \qquad \text{Equation 3}$$

where ψ is the system pressure sensitivity in mV/kPa, and N is the root-mean-squared (RMS) noise level in mV. To determine the NEP of the free-space microresonator sensors, a substitution method based on the use of a broadband laser ultrasound source (see below) and a calibrated reference sensor was used as follows. The pressure output of the laser ultrasound source was determined using a reference Fabry-Pérot (FP) ultrasound sensor of known pressure sensitivity and flat frequency response from 0.5 to 75MHz (-3dB). Since the source bandwidth (~70MHz) significantly exceeds that of the microresonator sensors, the signal measured by the reference FP sensor was digitally low pass filtered using a cut-off frequency equal to the -3dB bandwidth of the microresonator sensor under test. This yields the pressure *p* over the frequency range for which the microresonator response is flat – i.e. the above mentioned low frequency limit. The reference sensor was then replaced by the microresonator sensor and the measurement of the source output repeated under identical conditions including application of the same low-pass filter. Using this measurement and *p* then enabled ψ to be calculated. The noise N was measured by calculating the RMS value from a 100μs long segment of the filtered waveform taken from immediately before the arrival of the acoustic pulse without signal averaging. By measuring the noise simultaneously with the signal (in the same non-averaged waveform), it was ensured that the noise was accurately captured under realistic practical operating conditions. The NEP was then obtained from ψ and N using equation 3. Note that the above low pass filtering step applied to both reference and sensor measurements is equivalent to band-limiting the acoustic source so that its frequency content lies within the low frequency limit as defined above for an accurate representation of NEP. For additional verification, a calibrated 1MHz transducer (which is well within the low frequency limit of all the sensors) was also used to measure the NEP and found to be in close agreement.

The fibre microresonator sensor has a non-uniform frequency response (figure 3c) so its NEP was measured at a single acoustic frequency using a calibrated 3.5MHz planar transducer, over a 20MHz measurement bandwidth. The reference FP sensor and the 1MHz and 3.5MHz transducers were calibrated by comparison with a PVDF membrane hydrophone that had been calibrated with reference to a primary standard by the National Physical Laboratory, UK.

Frequency response measurements

Frequency response (figure 2a) was measured by comparison with a reference sensor of known frequency response characteristics as follows. Firstly, an averaged waveform in response to a broadband monopolar acoustic plane-wave (planar over a diameter of ≈1cm) was acquired using each microresonator sensor. The measurement was then repeated under identical conditions using a planar FP sensor[7] with a flat frequency response from 0.5 to 75MHz (-3dB)[21] that acted as a reference. This bandwidth significantly exceeds that of the microresonator sensors. It is therefore assumed that the reference FP sensor provides an accurate representation of the frequency spectrum of the incident acoustic wave over the frequency range of interest. The frequency response of each microresonator was then obtained by dividing the FFT (Fast Fourier Transform) of the recorded signal by that of the reference waveform. In the case of the fiber sensor (figure 3c), a different reference sensor was used with a still broader -3dB bandwidth of 130MHz.

Frequency-dependent directivity measurements

Directional response was measured by acquiring averaged signals in response to a laser-generated broadband monopolar acoustic plane-wave rotated about the sensor interrogation point. Signals were captured at discrete rotational increments of 0.5°. For display (figures 2b-c and 3d-e) the FFT of each signal was divided by that obtained at normal incidence and the resultant map of relative response as a function of frequency and angle was plotted. The fibre sensor directivity was acquired and processed in the same manner except that the source was fixed and the fiber sensor rotated about a fixed point in the acoustic field.

Laser-generated ultrasound sources

The laser ultrasound source used to measure NEP, frequency response and directivity comprised a thin layer of black spray-paint (PlastiKote® GLOSS SUPER) deposited on an 8mm thick, 2.5mm diameter polymethylmethacrylate (PMMA) substrate. This was illuminated with a large (>2cm) diameter laser beam emitted by a fibre-coupled 1064nm Q-switched laser (Minilite, Continuum Lasers or Big Sky Ultra, Quantel Laser) so as to photoacoustically generate a broadband (1-70MHz) monopolar ultrasonic plane-wave. The absolute pressure level was calculated using a planar Fabry-Pérot sensor with a theoretical -3dB bandwidth of 75MHz[7], the sensitivity of which was calibrated with reference to a primary standard, certified by the UK National Physics Laboratory.

The fibre laser ultrasound source used to acquire the data in figure 4d was a highly absorbing carbon nanotube and polydimethylsiloxane (PDMS) layer deposited on to the tip of a 200µm diameter optical fibre and irradiated with 1.5ns laser pulses at 1064nm[29,30].

Comparison with piezoelectric sensor sensitivity

The NEP of a 1mm diameter, 28µm thick PVDF needle hydrophone (Precision Acoustics) with a low noise preamplifier adjacent to the PVDF element was measured using the procedure outlined above for the fibre microresonator (see "noise equivalent pressure measurements"). The measured NEP was 55Pa (RMS) over a 20MHz measurement bandwidth. Assuming that sensitivity scales linearly with active area, a similar 2mm diameter PVDF sensor would therefore be expected to have an NEP of 13.75Pa over 20MHz or 3.1mPa/√Hz. As this is comparable to the measured NEP of the 100µm microresonator (figure 1), the 2mm diameter sensor was chosen as the basis for comparison when evaluating the directional response of the microresonator sensor (figure 2b).

Modelled directivity due to spatial averaging

The directional sensitivity $D(\theta)$, of a circular piezoelectric receiver of diameter 2mm (figures 2b-c and 3d-e), was modelled as that of a spatially averaging stiff disk[31]:

$$D(\theta) = \frac{2J_1(ka\sin\theta)}{ka\sin\theta} \qquad \text{Equation 4}$$

in which k is the acoustic wavenumber ($2\pi/\lambda$), a the element radius, and J_1 the first-order Bessel function.

OR-PAM excitation beam fluence

Due to the relatively low NA of the scan lens, the surface fluence was approximately 100mJ/cm^2 compared to the ANSI 20mJ/cm^2 limit. At the focus, where the irradiance is highest however, the fluence was 2J/cm^2 and comparable to that used in other OR-PAM in vivo imaging studies[23,32].

Supplementary information: Ultra-sensitive planoconcave optical microresonators for ultrasound sensing

James A. Guggenheim[1,], Jing Li[1], Thomas J. Allen[1], Richard J. Colchester[1], Sacha Noimark[2], Olumide Ogunlade[1], Ivan P. Parkin[2], Ioannis Papakonstantinou[3], Adrien Desjardins[1], Edward Z. Zhang[1], and Paul C. Beard[1]

[1]Department of Medical Physics and Biomedical Engineering, University College London, Gower Street, London, WC1E 6BT, UK
[2]Department of Chemistry, University College London, Gower Street, London, WC1E 6BT, UK
[3]Department of Electronic and Electrical Engineering, University College London, Gower Street, London, WC1E 6BT, UK

Additional imaging studies were performed to demonstrate the photoacoustic imaging performance of the microresonator sensors and compare it to that of the planar Fabry-Pérot (FP) etalon[1,2] sensor. The latter has been comprehensively characterized in terms of its acoustic characteristics and photoacoustic imaging performance[1,2] and thus provides a well-established benchmark for comparison.

Photoacoustic imaging in tomography mode using free-space planoconcave microresonator sensors.

Two studies were performed in which tissue phantoms were imaged in widefield photoacoustic tomography mode in order to compare the penetration depth and image quality of the planar FP sensor with that of the planoconcave microresonator sensors.

Penetration depth: 3 free-space planoconcave microresonator sensors representing the family of sensors presented figure 1 were used to image a deep phantom in order to investigate the penetration depth that could be achieved. The experimental arrangement is shown in supplementary figure 1(a) below. The tissue phantom was designed to be approximately tissue-realistic and deep (>4 cm) to provide an indicative estimate of the penetration depth that might be achievable when imaging biological tissues. It comprised 8 optically transparent polythene tubes filled with an absorbing dye with an absorption coefficient μ_a=3 cm^{-1} which is similar to that of blood (90% blood oxygen saturation) at 750nm[3]. The tubes were immersed in Intralipid with a reduced scattering coefficient μ'_s=6cm^{-1} and a μ_a=0.12cm^{-1} yielding an effective attenuation coefficient of μ_{eff}=1.5 cm^{-1} which is comparable to that of soft tissues at 750nm[3]. The phantom was illuminated with wide-field laser pulses emitted by a fibre-coupled 1064 nm Q-switched ND:YAG laser (Minilite, Continuum Lasers) with a pulse repetition frequency (PRF) of 20 Hz and a pulse-width of 6ns. The pulse energy at the fibre output was 14 mJ and the illuminated area at the liquid surface was ≈80 mm^2. The surface fluence was therefore approximately 18 mJ/cm^2, below the maximum permissible exposure for human skin[4]. To acquire an image, a single static sensor was used and the tissue phantom mechanically scanned in two dimensions (2D), thereby emulating a 2D array of identical sensors. The phantom was scanned over a total area of 41 mm × 12 mm in steps of 100 μm and 200 μm. Acoustic waveforms were acquired after each step by an oscilloscope (TDS5K, Tektronix) triggered by a photodiode.

Prior to image reconstruction, the recorded acoustic waveforms were filtered using a low pass filter with a -3dB cut-off equal to the -3dB bandwidth of the sensor. 3D Images were then reconstructed using a reconstruction algorithm based on time reversal[5]. Following reconstruction, images were cropped to a region of interest of volume 15 × 12 × 42 mm and subjected to a 1D fluence correction[6] to aid visualisation. The images were then rendered in 3D using Volview (version 3.4, Kitware) and plotted in supplementary figures 1(b-e). 2D cross-sections were taken through the centre

of the 3D images, mapped to a linear colour scale and plotted in supplementary figures 1(f-i). Finally, vertical line profiles were taken through the centres of the tubes in each of the 2D cross-sectional images and plotted in supplementary figures 1(j-m).

The images show that the planoconcave microresonator sensors provide increased penetration depth compared to the planar sensor. The penetration depth increase over the planar sensor is 10mm for the 100µm sensor and 16mm for the 250µm and 460µm sensors. Moreover, as the optical properties of the tissue phantom are tissue-realistic, these figures provide an approximate indication of the extent to which the higher sensitivity of the planoconcave microresonator sensors might translate to increased penetration depth when imaging biological tissues.

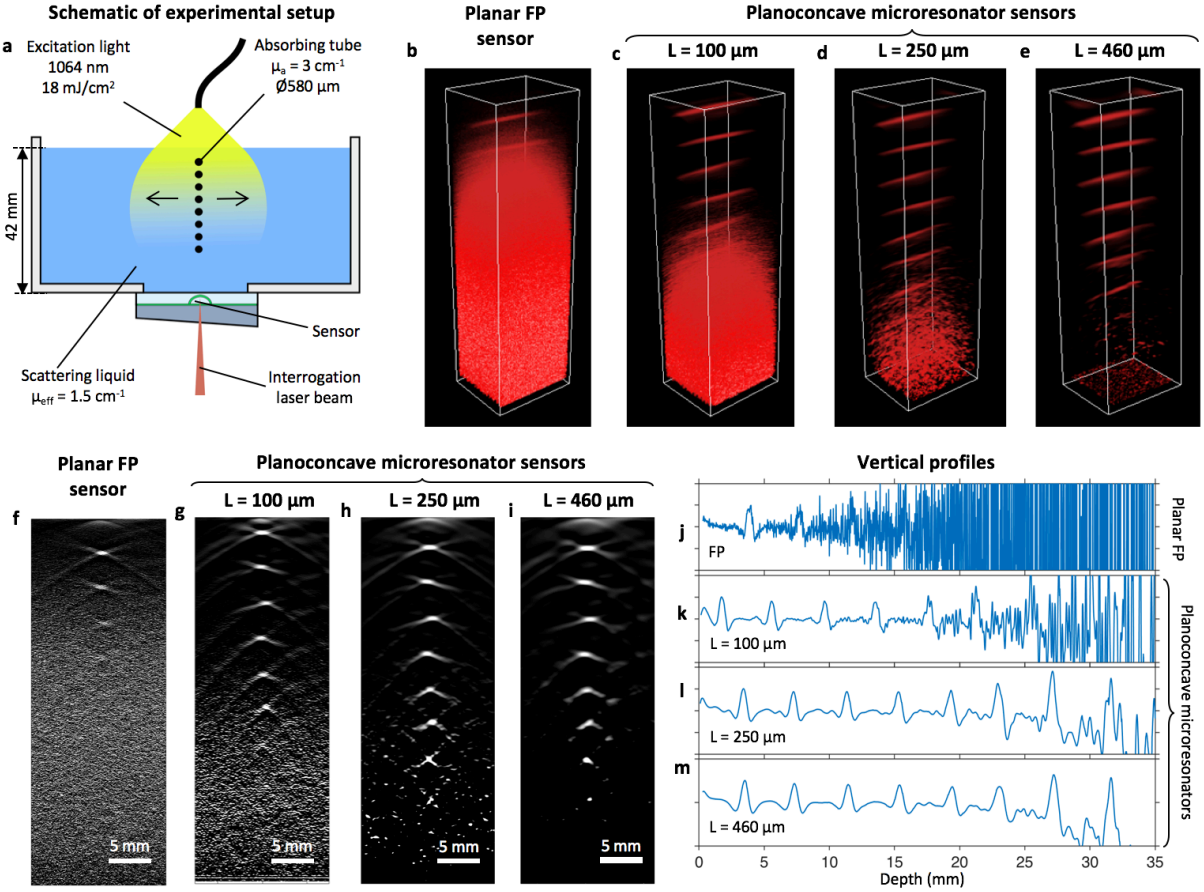

Supplementary figure 1 | Comparison of photoacoustic image penetration depth obtained using a planar FP sensor and 3 planoconcave microresonator sensors in tomography mode. (a) Schematic of the tissue phantom imaging setup. The phantom was composed of an optically scattering liquid (0.8% intralipid in DI water, μ_{eff} = 1.5 cm^{-1} at 1064 nm) with blood-vessel-like optically absorbing tubes (Indian ink solution, μ_a = 3 cm^{-1}, tube inner diameter Ø580 µm),. (**b-e**), 3D renderings of reconstructed images obtained with **(b)** the FP sensor and **(c)** 100 µm, **(d)** 250 µm and **(e)** 460 µm planoconcave microresonator sensors. **(f-i)**, 2D cross-sections taken through the centre of each reconstructed 3D image. **(j-m)**, vertical profiles through each cross-section.

Image quality. Supplementary figures 1(f-i) suggest that the image quality provided by the planoconcave microresonator sensors is similar to that provided by the FP planar sensor. However, compared to typical PA images obtained with the FP sensor[1] the images show significant artefacts (manifesting as "X" shaped features centred upon each tube). These are a consequence of the experimental conditions; a combination of limited-aperture effects and artefacts due to the acoustic impedance mismatch between the tube walls and the surrounding Intralipid suspension. Images were

therefore acquired with the phantom positioned closer to the sensor plane to reduce limited aperture effects and using tubes made of a different material with a reduced acoustic impedance mismatch.

The experimental arrangement is shown in supplementary figure 2(a) below. The phantom comprised a row of 3 tubes made of a fluoropolymer blend (THV604-725-5, Paradigm Optics) with an absorption coefficient of 6 cm^{-1} (still comparable to that of blood in the near infrared[3]). The row of tubes was located at a distance of 8.5 mm from the sensor. Imaging was performed as described above with a 130 µm microresonator and a planar FP for comparison. The resultant images are shown in supplementary figures 2(b-e).

The images are relatively artefact-free and provide a sharp, faithful representation of the three tubes. Moreover, the planoconcave microresonator image is practically indistinguishable from that of the FP with the only apparent difference being a clear improvement in SNR in the image acquired by the planoconcave microresonator consistent with its lower NEP. As in the case of the images, the profiles corresponding to the planoconcave microresonator and FP sensor are also very similar.

These results show that the planoconcave microresonator sensor mimics the excellent image quality that has previous been demonstrated using the planar FP sensor[1,2]. This is as expected since both sensor types provide similarly well behaved frequency response and directional characteristics and it is these characteristics that primarily define image quality.

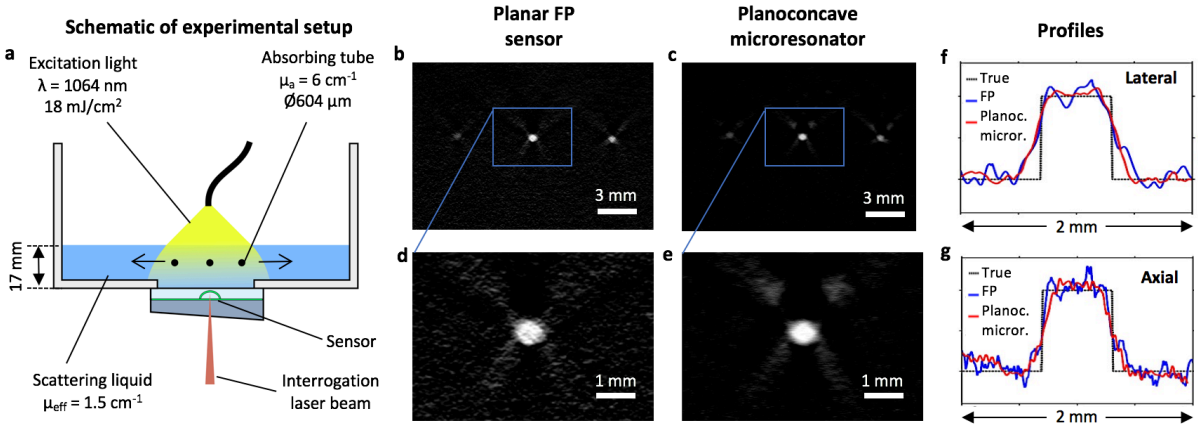

Supplementary figure 2 | Comparison of photoacoustic image quality obtained using a planar FP sensor and a planoconcave microresonator sensor in tomography mode. (a) Schematic of the imaging setup with the tissue phantom which was composed of an optically scattering liquid (0.8% intralipid, μ_{eff} = 1.5 cm^{-1} at 1064 nm) with 3 blood-vessel-like optically absorbing tubes (Indian ink solution, μ_a = 6 cm^{-1}, inner diameter Ø604 µm). **(b-c)**, 2D cross-sections taken through the reconstructed images obtained with **(b)** the FP sensor and **(c)** the 130 µm planoconcave microresonator sensor, **(d-e)**, zoomed in versions showing the central tube cross-section in detail. **(f)** lateral and **(g)** vertical line profiles taken through the central tube with the ground truth based on the known inner diameter of the tube.

ORPAM using fiber optic planoconcave microresonator sensors.

The performance of a fibre optic planoconcave microresonator sensor and a fiber optic planar FP sensor were compared using the OR-PAM configuration shown in figure 4(a). As in the tomography-mode examples above, a tissue phantom was imaged to provide a well-controlled comparison. The phantom was a leaf skeleton dyed using Indian ink to provide photoacoustic contrast. The resultant OR-PAM images are plotted in supplementary figures 3(a-b).

The image obtained with the planar FP sensor (fig. 3(a)) shows poor contrast due to its low sensitivity and a small field of view due to its limited directivity. By contrast, the image obtained with the planoconcave microresonator sensor shows much higher contrast due to its order of magnitude higher sensitivity and significantly larger field of view due to its wider directivity. Profiles were taken through both images at a region of relatively high contrast in the planar sensor image. These are plotted in supplementary figure 3(c). It is evident in the profiles that the image SNR is significantly

higher in that of the planoconcave microresonator compared to that of the planar sensor. Overall the data in supplementary figure 3 shows that the fibre-optic planoconcave microresonator sensor provides improved imaging performance in OR-PAM.

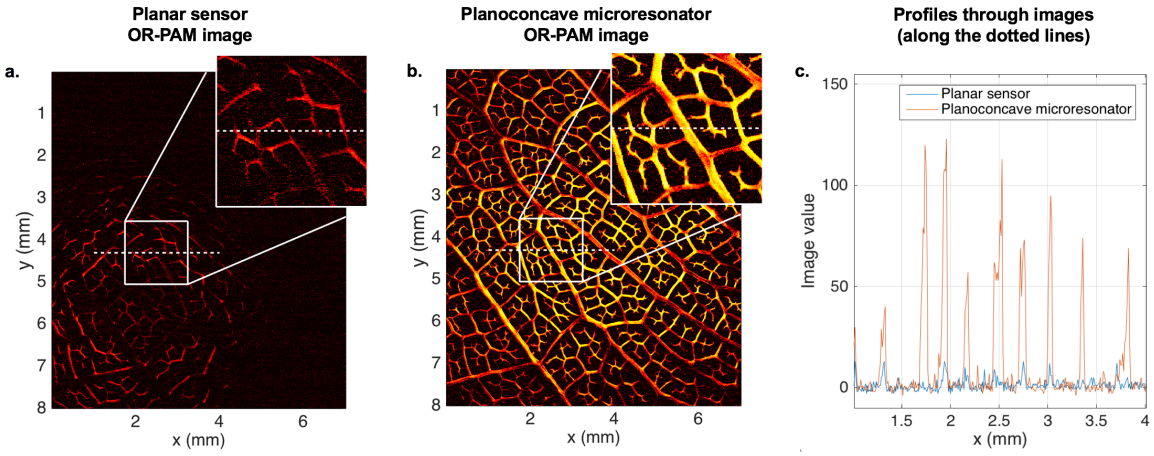

Supplementary figure 3 | Comparison of OR-PAM images obtained using (a) planar FP sensor and (b) planoconcave microresonator sensor with (c) profiles taken through the images at the location indicated by the dotted lines. Insets: zoomed in regions of the images at the area of highest intensity in the planar sensor image. The imaged sample was a phantom comprising a leaf skeleton dyed with black ink to provide photoacoustic contrast.

References

1. Jathoul, A. P. *et al.* Deep in vivo photoacoustic imaging of mammalian tissues using a tyrosinase-based genetic reporter. *Nat. Photonics* **9,** 239–246 (2015).
2. Zhang, E., Laufer, J. & Beard, P. Backward-mode multiwavelength photoacoustic scanner using a planar Fabry-Perot polymer film ultrasound sensor for high-resolution three-dimensional imaging of biological tissues. *Appl. Opt.* **47,** 561–577 (2008).
3. Jacques, S. L. Optical properties of biological tissues: a review. *Phys. Med. Biol.* **58,** 5007–5008 (2013).
4. Li, C. & Wang, L. V. Photoacoustic tomography and sensing in biomedicine. *Phys. Med. Biol.* **54,** R59-97 (2009).
5. Treeby, B. E., Zhang, E. Z. & Cox, B. T. Photoacoustic tomography in absorbing acoustic media using time reversal. *Inverse Probl.* **26,** 115003 (2010).
6. Treeby, B. E., Jaros, J. & Cox, B. T. Advanced photoacoustic image reconstruction using the k-Wave toolbox. in *Proceedings of SPIE* (eds. Oraevsky, A. A. & Wang, L. V.) **9708,** 97082P (2016).